Effect of Jahn−Teller Distortion in $La_{0.5}Sr_{0.5}MnO_3$ Cubes and Nanoparticles on the Catalytic Oxidation of CO and CH_4

Shuhui Liang, Fei Teng, G. Bulgan, and Yongfa Zhu*

Department of Chemistry, Tsinghua University, Beijing 100084, P. R. China

Received: June 25, 2007; In Final Form: August 28, 2007

$La_{0.5}Sr_{0.5}MnO_3$ cube and nanoparticle catalysts were synthesized by the hydrothermal and coprecipitation method, respectively. The catalytic performances for CO and CH_4 oxidation were evaluated, and the effect of Jahn−Teller distortion on the catalytic performance was elucidated. $La_{0.5}Sr_{0.5}MnO_3$ nanoparticle catalyst showed a higher activity than the cube catalyst for CO oxidation at a lower temperature. While the catalytic activity of the cubes significantly increased at higher temperature, the complete conversion temperatures for CO were both the same at 210 °C. The trend for CH_4 oxidation activity was similar to the trend observed for CO oxidation activity. The catalytic mechanism of CO oxidation over $La_{0.5}Sr_{0.5}MnO_3$ cubes is proposed that the adsorbed CO was oxidized by the lattice oxygen. Then, the chemisorbed oxygen over $La_{0.5}Sr_{0.5}MnO_3$ cubes was transformed into the lattice oxygen by MnO_6 octahedra to reinforce the consumed lattice oxygen. The catalytic performances of $La_{0.5}Sr_{0.5}MnO_3$ cubes and nanoparticles were mainly predominated by Jahn−Teller distortion of the catalysts.

1. Introduction

$La_{1-x}Sr_xMnO_3$ manganites with perovskite structure have been widely used as oxidation catalysts, cathode materials in solid-oxide fuel cells, and magnetic sensors.[1−4] Substitution of La^{3+} ion with Sr^{2+} generally results in a significant increase in activity for hydrocarbon combustion compared to that for $LaMnO_3$.[5−8] The partial or total substation of Sr^{2+} for La^{3+} in $La_{1-x}Sr_xMnO_3$ leads to the formation of Mn^{4+} or positive holes or oxygen vacancies in the perovskite structure. It is generally accepted that the enhancement of catalytic activity for $La_{1-x}Sr_xMnO_3$ is related to such a defective structure.[9,10] Most research has focused on the catalytic properties of various substituted quantities of Sr^{2+} ion. However, few investigations have been done on the effect of morphologies on the catalytic performances of $La_{1-x}Sr_xMnO_3$.[11,12] The catalysts with various morphologies such as the nanoparticle and nanorod show different catalytic activities because of the different distributions of catalytic active sites or crystal plane effects.[13−15] Jahn−Teller distortion can greatly influence the valence of Mn ion and the ability for charge transfer, which plays an important role in catalytic performance. The effect of Jahn−Teller distortion of MnO_6 octahedra in $La_{1-x}A_xMnO_3$ (A = Ca, Sr, Ba) samples on the magnetization property has been studied.[16,17] However, little work has been done to elucidate the relationship between Jahn−Teller distortion and catalytic properties. Recently, $La_{0.5}A_{0.5}MnO_3$ (A = Ca, Sr, Ba) cubes have been synthesized under hydrothermal conditions, and their magnetization properties have been determined.[18−20] Nevertheless, little research has been devoted to the study of the catalytic properties of these cubes up to now. Therefore, it is necessary to design $La_{0.5}Sr_{0.5}MnO_3$ samples with different morphologies (cube and nanoparticle) and reveal the effect of Jahn−Teller distortion on the catalytic performances.

In this work, $La_{0.5}Sr_{0.5}MnO_3$ catalysts with cube and nanoparticle structures were synthesized by hydrothermal and coprecipitation methods, respectively. The structures and catalytic performances of $La_{0.5}Sr_{0.5}MnO_3$ nanoparticles and cubes have been revealed by TEM (transmission electron microscopy), XRD (X-ray diffraction), CO- and CO_2-TPD (temperature-programming desorption), H_2-TPR (temperature-programmed reduction), Raman analysis, and CTL (cataluminescence). The effect of Jahn−Teller distortion of $La_{0.5}Sr_{0.5}MnO_3$ nanoparticles and cubes on CO and CH_4 catalytic oxidation was elucidated.

2. Experimental Section

2.1. Synthesis of $La_{0.5}Sr_{0.5}MnO_3$ Cubes and Nanoparticles. $La_{0.5}Sr_{0.5}MnO_3$ cubes were synthesized with $La(NO_3)_3{\cdot}6H_2O$, $SrCl_2{\cdot}6H_2O$, $KMnO_4$, $MnCl_2{\cdot}4H_2O$, and KOH. All the chemicals were analytical grade and used without purification. The molar ratios of La:Sr:Mn were kept at 0.5:0.5:1, based on the stoichiometric ratios of $La_{0.5}Sr_{0.5}MnO_3$. The mixture composition held ratios of $7Mn^{2+}$:$3MnO_4^{2-}$:$5Sr^{2+}$:$5La^{3+}$:1250KOH:$3256H_2O$.[18−20] The chemical reaction for the hydrothermal method can be formulated as $3\ KMnO_4 + 7\ MnCl_2 + 5\ La(NO_3)_3 + 5\ SrCl_2 + 36\ KOH = 10\ La_{0.5}Sr_{0.5}MnO_3 + 18\ H_2O + 15\ KNO_3 + 24\ KCl$. Typically, the reaction reagents were dissolved in 12 mL of deionized water by stirring for 0.5 h. The mixture was poured into a Teflon vessel (40 mL in volume) and subjected to hydrothermal treatment at 240 °C for 24 h. After cooling to room temperature naturally, the obtained products were filtered, washed several times with deionized water and ethanol, and dried in air at 50 °C for 24 h.

$La_{0.5}Sr_{0.5}MnO_3$ nanoparticles were prepared by the coprecipitation method. The solution mixture of $La(NO_3)_3{\cdot}6H_2O$, $SrCl_2{\cdot}6H_2O$, and $MnCl_2{\cdot}4H_2O$ at the stoichiometry above was precipitated using KOH and K_2CO_3 (1:1) mixed solution and pH was maintained at 11−12. The obtained products were washed several times with deionized water up to pH 7−8. The depositions were evaporated and completely dried at 80 °C

* To whom correspondence should be addressed. Tel: +86-10-62783586; fax: +86-10-62787601; e-mail: zhuyf@tsinghua.edu.cn.

10.1021/jp074934m CCC: $37.00
Published on Web 10/16/2007

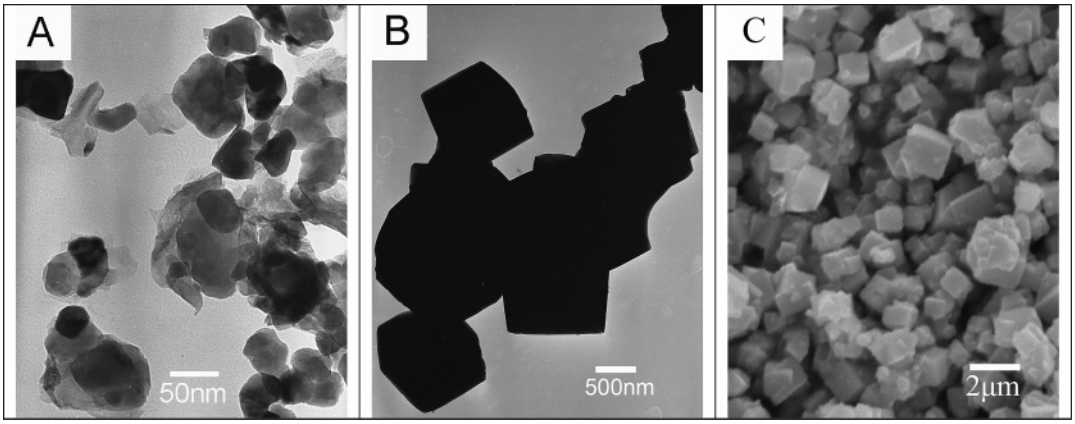

Figure 1. TEM and SEM images of $La_{0.5}Sr_{0.5}MnO_3$ catalysts. (A) The nanoparticles. (B, C) The cubes.

overnight in an oven. The obtained materials were crushed and calcined at 700 °C for 3 h under flowing air, and then the perovskite type oxide $La_{0.5}Sr_{0.5}MnO_3$ nanoparticles were obtained.

2.2. Characterization. The morphologies and sizes of $La_{0.5}Sr_{0.5}MnO_3$ samples were measured using a JEOL JEM-1200EX TEM with 100 kV accelerating voltage of electron beam and SEM (KYKY 2800) with 15 keV acceleration voltage and 1.2 nA current. The sample was characterized by XRD (Rigaku D/MAX-RB X-ray powder diffractometer), using Cu Kα radiation ($\lambda = 0.154$ nm), operating at 40 kV and 50 mA. BET (Brunauer−Emmett−Teller) surface areas of the catalysts were determined by N_2 adsorption at −196 °C using a Tristar 2010 Chemical Adsorption Instrument (Micromeritics). Raman spectra were acquired with a microscopic confocal Raman spectrometer (Renishaw, RM2000) using an Ar ion laser (514.5 nm) with 10 mW. ICP (inductively coupled plasma, Thermo Electron Corporation, IRIS Intrepid XSP) was used for the determination of metal element concentration.

2.3. H_2-TPR, CO-TPD, and O_2-TPD. A H_2-TPR (temperature-programmed reduction) experiment was performed on a conventional H_2-TPR instrument. A 0.1 g sample was placed in a quartz reactor and preheated under flowing 20% O_2 in He at 500 °C for 0.5 h. After cooling to room temperature, the sample was reduced with a 5% H_2/Ar mixture (30 mL min^{-1}), heating 10 °C min^{-1} up to 800 °C. H_2 was detected by a mass spectrometer.

A CO-TPD (temperature-programmed desorption) measurement was performed on the same setup used for TPR. A 0.1 g amount of catalyst was heated at 500 °C for 0.5 h in He flow to remove pollutants adsorbed on the catalyst. Under the flowing He gas (40 mL min^{-1}), the system was cooled naturally to room temperature. The sample was then saturated with CO at room temperature for 0.5 h. Excess adsorbate was removed by allowing the sample to remain under He flow until no significant amount of adsorbate could be detected. The temperature was ramped to 800 °C at a linear heating rate of 10 °C min^{-1}. A mass spectrometer was used to monitor the *m*/*e* ratios 28 (CO) and 44 (CO_2).

O_2-TPD measurements were carried out with a flow system using He as a carrier gas. Samples (0.1 g) were treated in an O_2 stream (20 mL min^{-1}) for 0.5 h at 500 °C. After they were cooled to room temperature, a He stream was substituted for an O_2 stream. Then the temperature was raised at a constant rate of 10 °C min^{-1} up to 800 °C and oxygen desorbed was detected by use of a mass spectrometer.

2.4. Catalytic Oxidation and Cataluminescence (CTL) Measurement. The reactions of CO and CH_4 oxidation were carried out in a flow system under atmospheric pressure. Catalyst (0.1 g) was loaded in a quartz reactor (inner diameter about 5 mm), with quartz beads packed at both ends of the catalyst bed. Before each run, the catalyst was flushed with air (100 mL min^{-1}) at 400 °C for 1 h in order to remove adsorbed species from the surface and then cooled to room temperature. For CO oxidation, a gas mixture of 2 vol % CO and 98 vol % air was fed into the catalyst bed at a gas hourly space velocity (GHSV) of 12000 h^{-1}. For CH_4 oxidation, a gas mixture of 1 vol % CH_4 and 99 vol % air was fed into the catalyst bed at a flow rate of 100 mL min^{-1}. The compositions of outlet gases were analyzed by an on-line gas chromatography with a GDX-403 GC-column (1.5 m × 4 mm, 100 °C) and a hydrogen flame ionization detector (FID).

The catalyst was sintered as a layer with 0.2 mm thickness on the heating tube that was put into a quartz tube of an inner diameter 12 mm. Comparison of CTL intensity from $La_{0.5}Sr_{0.5}MnO_3$ nanoparticles and cubes for CO oxidation was made after flow injection of 50 mL of pure CO gas (>99.0%) in an air carrier gas with a flow rate of 100 mL min^{-1} and a bandpass filter of 640 nm.[21] The consequent CTL intensity was directly measured with a BPCL ultraweak chemiluminescence analyzer (made by Biophysics Institute of Chinese Academy of Science in China).

3. Results

3.1. Morphology and Structure of $La_{0.5}Sr_{0.5}MnO_3$ Catalysts. Figure 1 shows TEM and SEM images of $La_{0.5}Sr_{0.5}MnO_3$ samples. Figure 1A indicated that the grain sizes of $La_{0.5}Sr_{0.5}MnO_3$ particles ranged from 40 to 80 nm. Figure 1B and 1C showed that the sample consisted of a cube-shaped crystallite. The average diameter of the cube catalyst was mainly in the range of 0.8−1.5 μm.

Figure 2 shows XRD patterns of $La_{0.5}Sr_{0.5}MnO_3$ catalysts. No shift of the diffraction peaks was observed for $La_{0.5}Sr_{0.5}MnO_3$ cubes and nanoparticles, and all diffraction peaks of the samples were indexed to pseudo-cubic perovskite structure ($a = 0.3849(1)$ nm). The diffraction peaks of $La_{0.5}Sr_{0.5}MnO_3$ nanoparticles were clearly broader than those of the cubes, indicating that the particles were nanocrystallite. ICP elemental analysis indicated that the compositions of the catalysts were close to the stoichiometric ratios of $La_{0.5}Sr_{0.5}MnO_3$ (La:Sr:Mn = 0.45:0.48:1 in the cubes and La:Sr:Mn = 0.56:0.52:1 in the nanoparticles). The mass ratios of Mn ions in the cubes and nanoparticles were accurate within ±5% of the value shown. In addition, the BET surface areas of $La_{0.5}Sr_{0.5}MnO_3$ nanoparticles and cubes were 9.28 and 4.50 m^2/g, respectively. The

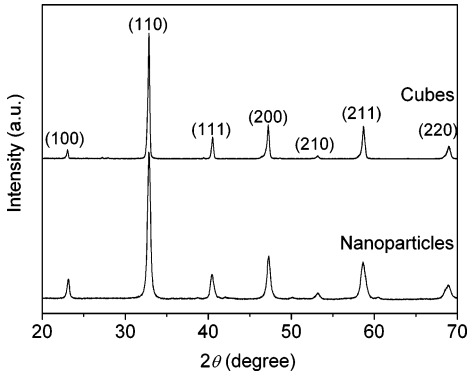

Figure 2. XRD patterns of $La_{0.5}Sr_{0.5}MnO_3$ nanoparticles and cubes.

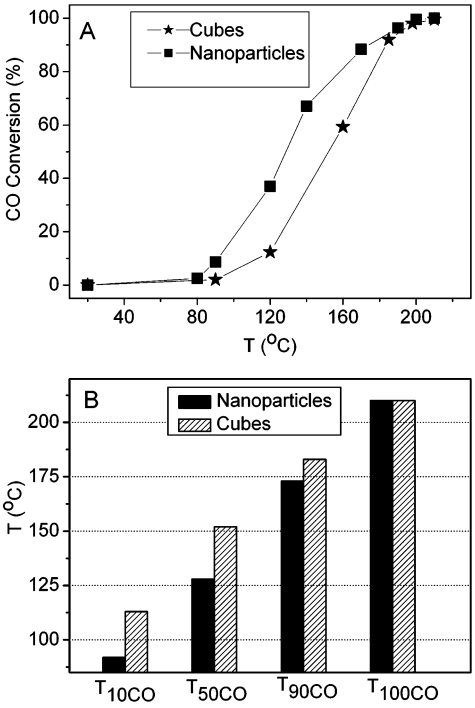

Figure 3. (A) Conversion of CO over $La_{0.5}Sr_{0.5}MnO_3$ nanoparticles and cubes. (B) The T_{10CO}, T_{50CO}, T_{90CO} and T_{100CO} of $La_{0.5}Sr_{0.5}MnO_3$ catalysts. T_{10CO}, T_{50CO}, T_{90CO}, and T_{100CO} are the temperatures of CO conversion 10%, 50%, 90%, and 100%, respectively.

adsorption average pore diameter of the cubes (24.9 nm) was larger than that of the nanoparticles (17.4 nm).

3.2. Catalysis Performance. The activities of $La_{0.5}Sr_{0.5}MnO_3$ cube and nanoparticle catalysts for CO oxidation were shown in Figure 3A, and the details are shown in Figure 3B. The catalytic activity of the nanoparticles was much higher than that of the cubes from 80 to 160 °C. For the nanoparticles, T_{10CO} (the temperature of CO conversion 10%) was 92 °C, but T_{10CO} was 113 °C for the cubes. T_{50CO} and T_{90CO} (the temperatures of CO conversion 50% and 90%, respectively) for the nanoparticles decreased 24 and 10 °C compared to those for the cubes, respectively. However, the catalytic activity of the cubes remarkably increased when the temperature was above 160 °C. The complete conversion temperatures for $La_{0.5}Sr_{0.5}MnO_3$ nanoparticle and cube catalysts were both 210 °C.

Figure 4A and 4B show the activities of $La_{0.5}Sr_{0.5}MnO_3$ catalysts for CH_4 oxidation. Here, the temperatures at 10%, 50%, and 90% conversions of CH_4 were described as T_{10CH_4}, T_{50CH_4}, and T_{90CH_4}, respectively. T_{10CH_4}, T_{50CH_4}, and T_{90CH_4} for the nanoparticles decreased 66, 42, and 18 °C compared to those for the cubes. The catalytic activity of the nanoparticles was much higher than that of the cubes at lower temperature, whereas the catalytic activity of the cubes significantly increased at higher temperature. The differences in catalytic activities for the $La_{0.5}Sr_{0.5}MnO_3$ nanoparticles and cubes for CH_4 oxidation followed a similar trend to that observed for CO catalytic oxidation.

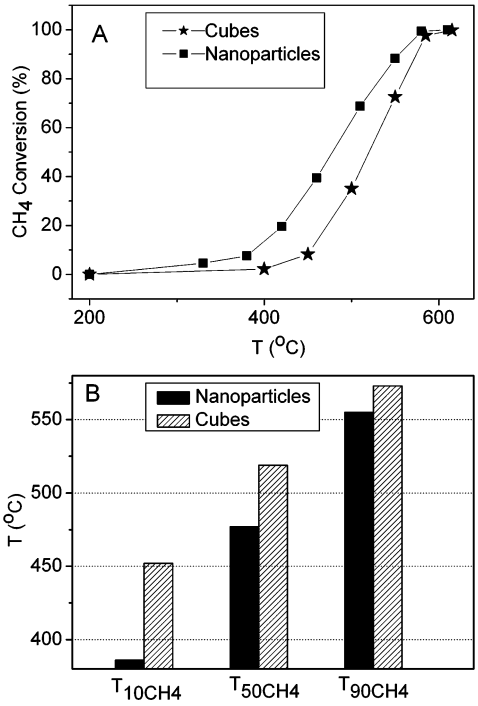

Figure 4. (A) Conversion of CH_4 over $La_{0.5}Sr_{0.5}MnO_3$ samples. (B) The T_{10CH_4}, T_{50CH_4}, T_{90CH_4} of $La_{0.5}Sr_{0.5}MnO_3$ catalysts. T_{10CH_4}, T_{50CH_4}, T_{90CH_4} are the temperatures of CH_4 conversion 10%, 50%, and 90%, respectively.

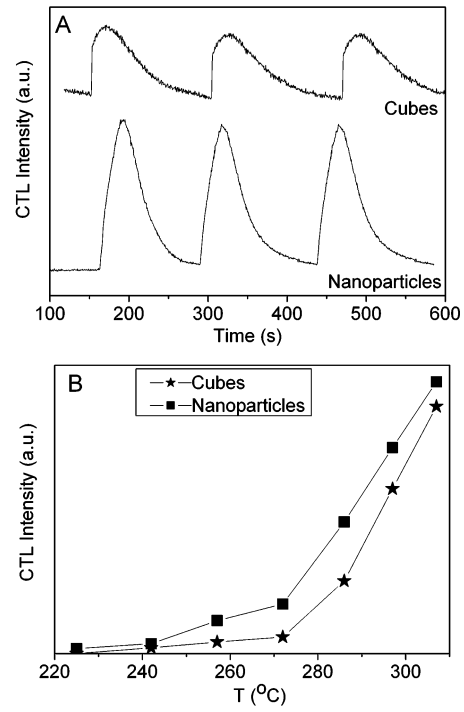

Figure 5. (A) CTL response for three consecutive injections of CO on $La_{0.5}Sr_{0.5}MnO_3$ nanoparticles and cubes at 255 °C. (B) CTL responses to CO on both catalysts at different temperatures.

3.3. CTL Properties. Figure 5A shows CTL profiles of $La_{0.5}Sr_{0.5}MnO_3$ samples in response to CO at 255 °C. The CTL intensities of $La_{0.5}Sr_{0.5}MnO_3$ nanoparticles were much higher than those of cubes. The response peaks over the nanoparticles

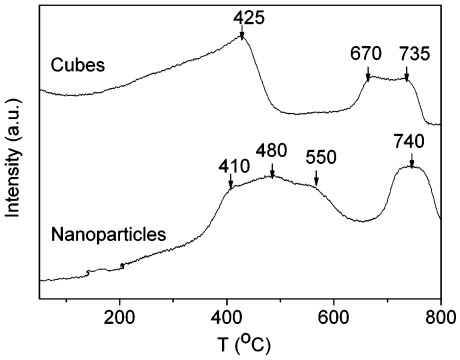

Figure 6. H_2-TPR profiles of $La_{0.5}Sr_{0.5}MnO_3$ nanoparticles and cubes.

TABLE 1: The Relative Consumed Amounts of H_2 for the $La_{0.5}Sr_{0.5}MnO_3$ Catalysts (peak area of per g catalyst)

	peak area of H_2 ($\times 10^8$) g^{-1}/°C	
catalyst	$T < 620$	$620 < T < 800$
Cubes	1.71	0.62
nanoparticles	1.67	0.64

were sharp, whereas they were broad bands over the cubes. It is generally accepted that the released energy is absorbed by CO_2 during CO oxidation on the surfaces of $La_{0.5}Sr_{0.5}MnO_3$ catalysts, forming excited CO_2* intermediates.[21] The excited intermediates can decay from the excited state to the ground state with luminescence.[22,23] CTL data at 255 °C indicated that the CO_2* intermediate could rapidly form and decay over $La_{0.5}Sr_{0.5}MnO_3$ nanoparticles, but the formation and decay of CO_2* over the cubes both was slightly slow. This may be partly because of the strong interaction bonds between the cubes and CO/CO_2 molecules. Effect of temperature on CTL intensity over $La_{0.5}Sr_{0.5}MnO_3$ catalysts is shown in Figure 5B. CTL intensities increased with the increased temperatures over both catalysts. The change trend of CTL intensities with temperatures was consistent with the change trend of the catalytic activities for CO oxidation over $La_{0.5}Sr_{0.5}MnO_3$ catalysts. CTL intensity of the nanoparticles was much higher than that of the cubes at lower temperature, whereas CTL intensity of the cubes remarkably increased at higher temperature. CTL response to CO also demonstrated the catalytic performances of $La_{0.5}Sr_{0.5}MnO_3$ nanoparticles and cubes for CO oxidation.[21]

3.4. Reducibility. H_2-TPR profiles of $La_{0.5}Sr_{0.5}MnO_3$ catalysts were performed to investigate the relative reducibility of the catalysts, as shown in Figure 6 and Table 1. Both profiles showed two clear reduction regions in 150−620 and 620−800 °C. The reduction peak of $La_{0.5}Sr_{0.5}MnO_3$ samples in the range of 150−620 °C was broad and asymmetric toward the lower temperature side. The nanoparticles showed a major peak about at 480 °C associated with two obvious shoulders at 410 and 550 °C. For the cubes, a major peak at about 425 °C can be distinguished. The shoulder placed at a slightly lower temperature (410 °C) can be assigned to the removal of the nonstoichiometric excess oxygen accommodated within the lattice.[24] The H_2-TPR major peak at 480 and 425 °C can be attributed to the reduction of Mn^{4+} to Mn^{3+} on $La_{0.5}Sr_{0.5}MnO_3$ nanoparticles and cubes, respectively. The shoulder at 550 °C on the nanoparticles may be due to a single electron reduction of Mn^{3+} located in coordination-unsaturated microenvironments.[25] The perovskite structure of $La_{0.5}Sr_{0.5}MnO_{3-x}$ sample was still preserved after the partial reduction (Mn^{4+} to Mn^{3+}) in the range of 150−620 °C.[25] The peaks at a higher temperature region of 620−800 °C (650−800 °C and 620−760 °C for $La_{0.5}Sr_{0.5}MnO_3$ nanoparticles and cubes) corresponded to the reduction of the remaining Mn^{3+} to Mn^{2+}. The color of the samples, initially black, became gray after the H_2-TPR run, suggesting that these new phases were present. XRD diffraction patterns (Figure 7A) demonstrated the breakdown of the perovskite structure and formation of discrete oxide phases such as La_2MnO_4, SrO, $SrMnO_3$, and MnO after H_2-TPR.[26] The peak areas of per g catalyst in H_2-TPR profiles can indicate relative consumption amounts of H_2 and to some extent reflect the thermally desorbed quantity of oxygen over $La_{0.5}Sr_{0.5}MnO_3$ cubes and nanoparticles. The desorbed quantity of oxygen mainly corresponding to the reduction of Mn^{4+} to Mn^{3+} and the removal of the nonstoichiometric excess oxygen accommodated within the lattice on the $La_{0.5}Sr_{0.5}MnO_3$ cubes (peak area of H_2, 1.71×10^8 g^{-1}) was larger than that on the nanoparticles (peak area of H_2, 1.67×10^8 g^{-1}). These two samples desorbed similar amounts of oxygen corresponding to the reduction of the remaining Mn^{3+} to Mn^{2+}. The reduction temperatures of Mn^{4+} to Mn^{3+} and Mn^{3+} to Mn^{2+} in $La_{0.5}Sr_{0.5}MnO_3$ cubes were obviously lower than those in the nanoparticles. H_2-TPR results indicated that the Mn-component in $La_{0.5}Sr_{0.5}MnO_3$ cubes can be more easily reduced than those in the nanoparticles. Therefore, the release of oxygen over the cubes was easier compared to the nanoparticles in a reducing environment.

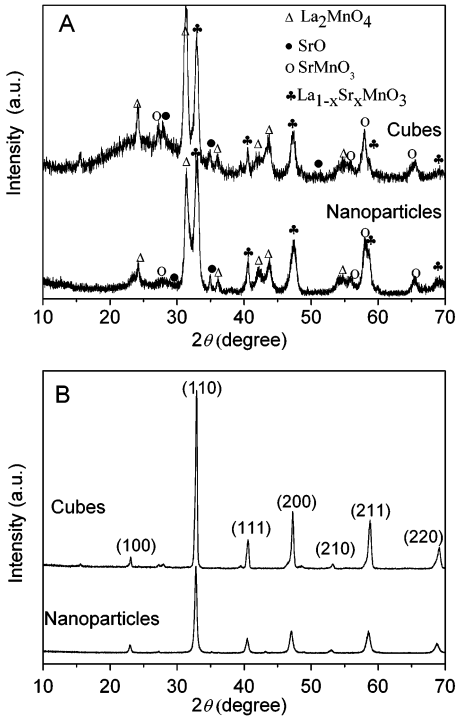

Figure 7. (A) XRD patterns of $La_{0.5}Sr_{0.5}MnO_3$ nanoparticles and cubes after the H_2-TPR run. (B) XRD patterns after the O_2-TPD run.

3.5. CO and O_2 Adsorption and the Active Site. CO-TPD was performed to explore CO adsorption on $La_{0.5}Sr_{0.5}MnO_3$ catalysts, as shown in Figure 8. Some adsorption CO was oxidized by nonstoichiometric oxygen and lattice oxygen of $La_{0.5}Sr_{0.5}MnO_3$ samples in the process of CO-TPD, and it desorbed in the form of CO_2 (Figure 8A). For $La_{0.5}Sr_{0.5}MnO_3$ nanoparticles, six CO_2 desorption peaks (143, 237, 312, 372, 475, and 650 °C) were observed from 140 °C up to 800 °C, whereas only one strong broad CO_2 desorption peak at higher temperature 700 °C and a tail peak extending from 760 °C up to 800 °C (where the experiment was stopped) were observed for $La_{0.5}Sr_{0.5}MnO_3$ cubes. Differences were also observed in CO desorption profiles of $La_{0.5}Sr_{0.5}MnO_3$ catalysts, as shown in Figure 8B. One sharp peak at 145 °C and one gradual broad

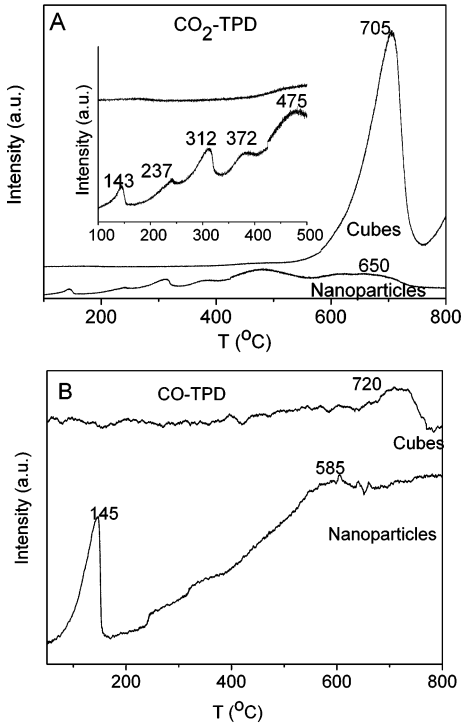

Figure 8. TPD spectra after CO adsorption over $La_{0.5}Sr_{0.5}MnO_3$ nanoparticles and cubes. (A) TPD of CO_2. (B) TPD of CO.

TABLE 2: The Relative Amounts of CO and CO_2 Desorbed from the $La_{0.5}Sr_{0.5}MnO_3$ Catalysts (peak area of per g catalyst)

	peak area of CO ($\times 10^4$) g^{-1}/ °C		peak area of CO_2 ($\times 10^4$) g^{-1}/°C	
catalyst	T < 500	500 < T < 800	T < 500	500 < T < 800
Cubes	0	24.6	0	87.2
nanoparticles	41.0	24.2	9.5	6.9

peak at 585 °C appeared for $La_{0.5}Sr_{0.5}MnO_3$ nanoparticles. Only one broad peak existed at higher temperature 720 °C for $La_{0.5}Sr_{0.5}MnO_3$ cubes. The desorption peak of CO at much higher temperatures indicated that the adsorption bond strength between CO and $La_{0.5}Sr_{0.5}MnO_3$ cubes was stronger.[27]

The peak areas of CO_2 or CO desorption can indicate relative desorption amounts of CO_2 or CO over $La_{0.5}Sr_{0.5}MnO_3$ cubes and nanoparticles.[28] We integrated the peak areas (per g catalyst) of CO and CO_2 and summarized the results in Table 2. The total adsorption amounts of CO on $La_{0.5}Sr_{0.5}MnO_3$ samples were consistent with the desorption amounts of CO_2 and CO. At the temperatures below 500 °C, the peak areas of desorption CO and CO_2 on the nanoparticles are both much larger than those on the cubes. Therefore, the total adsorption amounts of CO on the nanoparticles were much larger than those on the cubes, indicating that the nanoparticles could provide more active sites than the cubes at the lower temperatures.[29,30] Above 500 °C, the desorption peak area of CO_2 on the cubes was about 12.6 times larger than that on the nanoparticles, and the desorption peak area of CO on the nanoparticles was similar to that on the cubes. So the total adsorption amounts of CO on the cubes were much larger than those on the nanoparticles above 500 °C, suggesting that the cubes had many more active sites than the nanoparticles at the higher temperatures.

TPD spectra of O_2 over both $La_{0.5}Sr_{0.5}MnO_3$ catalysts are shown in Figure 9. It is generally accepted that the desorption peaks of oxygen at lower temperatures result from the oxygen

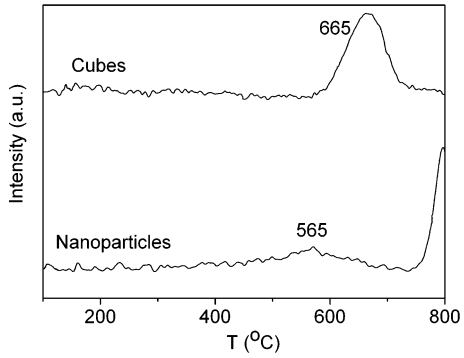

Figure 9. O_2-TPD profiles of $La_{0.5}Sr_{0.5}MnO_3$ nanoparticles and cubes.

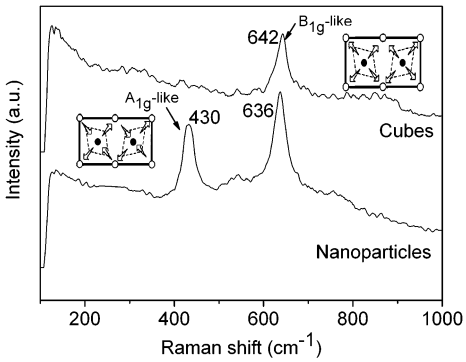

Figure 10. Raman spectra of $La_{0.5}Sr_{0.5}MnO_3$ nanoparticles and cubes. Small open circles are oxygen ions and small black circles are manganese ions in A_{1g}-like and B_{1g}-like modes.

TABLE 3: The Relative Desorbed Amounts of O_2 from the $La_{0.5}Sr_{0.5}MnO_3$ Catalysts (peak area of per g catalyst)

	peak area of O_2 ($\times 10^4$) g^{-1}	
catalyst	α oxygen at <600 °C	β oxygen at 600-800 °C
cubes	8.8	24.2
nanoparticles	0	67.0

adsorbed on the catalyst surface, which is described as α oxygen. The desorption peaks of oxygen at higher temperatures can be referred to the reduction of Mn^{4+} ions to lower valences accompanied by the evolution of equivalent lattice oxygen, which is described as β oxygen.[31−33] α and β oxygen desorption peaks appeared on the profile of O_2 desorption of the nanoparticle sample. The α oxygen desorption peak was broad and small at lower temperature, 565 °C, while the β oxygen desorption peak was strong, extending from 740 up to 800 °C (where the experiment was stopped). However, only one strong and broad O_2 desorption peak at relatively lower temperature, 665 °C, was observed for $La_{0.5}Sr_{0.5}MnO_3$ cubes. XRD results after O_2-TPD showed that both catalysts still retained the perovskite phase structures (Figure 7B). On the basis of H_2-TPR results, Mn^{4+} ions in the cubes can be reduced at slightly lower temperature than those in the nanoparticles. So the O_2 desorption peak at 665 °C may be mainly attributed to the reduction of Mn^{4+} to Mn^{3+} in the cubes. The relative desorbed amounts of O_2 from the $La_{0.5}Sr_{0.5}MnO_3$ are summarized in Table 3. The desorption amount of O_2 for the cubes was about 7.6 times larger than that of α oxygen for the nanoparticles. The different CO and O_2 desorption properties and the reducibility of $La_{0.5}Sr_{0.5}MnO_3$ nanoparticles and cubes may also be related to their different defect structures.

3.6. Defect Structure. Figure 10 shows Raman spectra of $La_{0.5}Sr_{0.5}MnO_3$ catalysts. Two main peaks at 430 and 636 cm^{-1} were observed for $La_{0.5}Sr_{0.5}MnO_3$ nanoparticles, but the peak

at 430 cm^{-1} cannot be observed for $La_{0.5}Sr_{0.5}MnO_3$ cubes, and only one peak at 642 cm^{-1} appeared. The peaks at 430 cm^{-1} and about 640 cm^{-1} (636, 642 cm^{-1}) can be attributed to A_{1g}-like and B_{1g}-like vibrational modes involving Mn−O stretching vibration motions of MnO_6 unit, respectively.[34] A_{1g}-like and B_{1g}-like modes resulted from A_{1g} and B_{1g} modes of $LaMnO_3$ in the orthorhombic D_{2h}^{16} phase.[35−38] Raman spectra of $La_{0.5}Sr_{0.5}MnO_3$ nanoparticles contained two vibration modes (A_{1g}-like and B_{1g}-like). The A_{1g}-like mode reflected extension and compression of Mn−O bond pairs, which was directly correlated with Jahn−Teller distortion. The B_{1g}-like vibration mode was related to the extension of Mn−O in MnO_6 units. $La_{0.5}Sr_{0.5}MnO_3$ cubes did not show the band at 430 cm^{-1}, which resulted from the smaller Jahn−Teller distortion of the ideal cubic structure. The coordination oxygen atoms of $Mn^{3+}O_6$ can form a Jahn−Teller distorted octahedral, whereas Mn^{4+} ions in $Mn^{4+}O_6$ units have almost undistorted coordination.[35] The degree of Jahn−Teller distortion in the cubes was smaller. So the ratio of Mn^{3+}/ Mn^{4+} in $La_{0.5}Sr_{0.5}MnO_3$ cubes was less than that in the nanoparticles. The dz^2 orbitals of Mn^{3+}, associated with long Mn^{3+}−O bonds in the Jahn−Teller distorted $Mn^{3+}O_6$ octahedra, would order, forming zigzag chains in the *ac* plane.[39] This ordering would entail displacements of $Mn^{4+}O_6$ octahedra. Charge ordering was accompanied by orbital ordering, so the mobility of charge carriers in the complex with Jahn−Teller distortion was restricted to some extent. The absence of the A_{1g}-like mode for $La_{0.5}Sr_{0.5}MnO_3$ cubes (small Jahn−Teller distortion) was consistent with the result of the facile mobility of Mn^{3+}→Mn^{4+}charge carriers. It can be expected that the different Jahn−Teller distortion degrees affect the adsorption of reacting molecules and the catalytic activities of $La_{0.5}Sr_{0.5}MnO_3$ catalysts.

4. Discussion

Why are the catalytic activities for CO and CH_4 oxidation different for $La_{0.5}Sr_{0.5}MnO_3$ nanoparticles and cubes? It's necessary to elucidate the key factors that govern the catalytic activities of $La_{0.5}Sr_{0.5}MnO_3$ samples. Here, the CO oxidation reaction over $La_{0.5}Sr_{0.5}MnO_3$ catalysts is used as a probe to reveal the essential factors that influence the catalytic performance.

4.1. Active Site and Catalytic Activity for CO Oxidation. In general, BET surface area is a main factor that may influence the activity of a catalyst. The BET surface area of $La_{0.5}Sr_{0.5}MnO_3$ nanoparticles is about 2 times as large as that of the cubes. However, the catalytic activity for CO oxidation of the nanoparticles is similar to that of the cubes above 180 °C, and the complete oxidation temperatures are both 210 °C. The results indicate that the catalytic activities are not significantly correlated with BET surface areas. The difference between $La_{0.5}Sr_{0.5}MnO_3$ nanoparticles and cubes in activity for CO oxidation may be related to their active sites and defect structures which can greatly influence the catalytic performance. Further investigation is taken to explore the main factors governing CO catalytic oxidation.

The catalytic property is governed by the active sites on the surface of the catalyst.[13] Based on CO- and CO_2-TPD data, $La_{0.5}Sr_{0.5}MnO_3$ nanoparticles have many more active sites than the cubes at lower temperature. The higher catalytic activity of the nanoparticles for CO oxidation below 160 °C can be attributed to the active sites. CO- and CO_2-TPD results indicate that $La_{0.5}Sr_{0.5}MnO_3$ cubes can provide more active sites at higher temperature. The catalytic activity of the cubes can significantly increase above 160 °C. At 210 °C, the nanoparticle and cube catalysts both completely convert CO into CO_2. Thus, the numbers and distribution of active sites may be the main factor that influences the activities of $La_{0.5}Sr_{0.5}MnO_3$ catalysts for CO oxidation.

However, why do $La_{0.5}Sr_{0.5}MnO_3$ cubes have more catalytic activity sites for CO oxidation at higher temperatures? What factors determine that the nanoparticles have more catalytic activity sites at lower temperatures? Structure may be related to these properties. Jahn−Teller distortion has been investigated to explore the above questions.

4.2. Jahn−Teller Distortion and CO Chemisorption. CO chemisorption is directly related to the catalytic reaction over $La_{0.5}Sr_{0.5}MnO_3$ samples.[12] It is an activated process for CO oxidation over the catalysts. Mn ions act as active centers for CO chemisorption.[12] The interaction between Mn ions and CO molecules can be modeled by crystal field theory. CO 5σ electrons and empty $2\pi^*$ orbitals can coordinate with d orbitals and d electrons of Mn ions, respectively. CO 5σ electrons donate electrons to coordinate with MnO_6 species possessing empty e_g (dz^2) orbitals. The empty $2\pi^*$ orbitals of CO molecules show some P orbital properties. Therefore, the t_{2g} (dxy, dyz, or dxz) electrons of Mn ions can hold to the empty $2\pi^*$ orbitals of CO, forming feedback π bond. It not only increases the coordination bond strength (Mn−CO) but also decreases the bond strength of C−O among CO molecules.[12] The chemisorption of CO onto the catalysts involves the way in which CO attaches to the coordination sites of Mn ions. Here, CO and Mn sites function as Lewis base sites and Lewis acid sites, respectively. Jahn−Teller distortion may be the main factor that influences the properties of the Lewis acid.[40] The small degree of Jahn−Teller distortion of $La_{0.5}Sr_{0.5}MnO_3$ cubes results in the lower ratio of Mn^{3+}/Mn^{4+} and the enhancement of charge-transfer Mn^{3+}→Mn^{4+}. Therefore, the average positive charge of Mn ions is higher, and the average radius of Mn ions is smaller in the cubes than those in the nanoparticles. This makes the coordination bond between Mn and CO molecule strong. Therefore, the cubes can desorb more CO at higher temperatures. The large degree of Jahn−Teller distortion of the nanoparticles greatly reduces the strength between Mn ions and CO molecules. More CO molecules can be provided by $La_{0.5}Sr_{0.5}MnO_3$ nanoparticles at lower temperature. Jahn−Teller distortion is the essential factor that governs CO chemisorption on $La_{0.5}Sr_{0.5}MnO_3$ nanoparticles and cubes.

Furthermore, the small degree of Jahn−Teller distortion in the cubes enhances the charge-transfer Mn^{3+}→Mn^{4+}. It allows the cubes to be reduced at lower temperature compared with the nanoparticles (This result is consistent with H_2-TPR and O_2-TPD results).

4.3. Mechanism of CO and CH_4 Catalytic Oxidation. On the basis of CO- and CO_2-TPD, H_2-TPR, O_2-TPD, Raman data, and the relationship between catalytic activities of $La_{0.5}Sr_{0.5}MnO_3$ samples and active sites, CO catalytic oxidation over $La_{0.5}Sr_{0.5}MnO_3$ cubes may involve lattice oxygen.[41] The catalytic oxidation process may be described as follows:

$$CO\ (g) \rightarrow CO\ (ads)$$

$$CO\ (ads) + O\ (lattice) \rightarrow CO_2\ (ads)$$

$$CO_2\ (ads) \rightarrow CO_2\ (g)$$

$$O_2\ (g) \rightarrow O_2\ (ads) \rightarrow O\ (ads) \rightarrow O\ (lattice)$$

The mechanism of CO oxidation over $La_{0.5}Sr_{0.5}MnO_3$ cubes involves adsorbed CO on Mn site reacting with the lattice oxygen, whereas the chemisorbed oxygen transforms into the lattice oxygen to reinforce the consumed lattice oxygen.[42] CO chemisorption, the supply of lattice oxygen, and the transformation of adsorption oxygen into lattice oxygen are the three main factors that govern the catalytic properties of $La_{0.5}Sr_{0.5}MnO_3$ cubes. The high catalytic activity of the cubes above 160 °C may be the result of the following three factors. First, the bond strength between the cubes and CO is strong. The cubes just can provide active CO at significantly higher temperatures. Second, the cubes can be reduced (provide plenty of lattice oxygen) at slightly higher temperatures based on the H_2-TPR and O_2-TPD results. Third, it is proposed that oxygen transformation occurs through MnO_6 octahedral charge transfer, as shown in Figure 11.[43] The mobility of $Mn^{3+} \rightarrow Mn^{4+}$ charge carriers is enhanced in the cubes and the charges shift is accelerated at higher temperatures. Therefore, it is easy for the cubes to reinforce lattice oxygen by the charge transfer between MnO_6 octahedral. In conclusion, Mn site of $La_{0.5}Sr_{0.5}MnO_3$ cubes is the active center for CO chemisorption and the lattice oxygen is active oxygen species.

Though the mobility of $Mn^{3+} \rightarrow Mn^{4+}$ charge transfer is slow, the nanoparticles show higher catalytic activity for CO oxidation below 160 °C. The CO oxidation reaction on the nanoparticles may proceed via the interaction between the adsorbed CO and the gaseous oxygen or adsorption oxygen. CO chemisorption is the main factor that influences the catalytic activity of the nanoparticles. The large degree of Jahn−Teller distortion in the nanoparticles greatly reduces the bond strength between Mn ions and CO molecules, and more active CO molecules can be provided at lower temperature. Therefore, the nanoparticles show higher catalytic activity below 160 °C.

Methane oxidation on metal oxides is known to follow a redox mechanism.[44−46] The oxidation of methane takes place by means of the adsorption and lattice oxygen from the catalyst, even in the presence of gaseous oxygen.[47] The catalytic activities of $La_{0.5}Sr_{0.5}MnO_3$ catalysts are determined mainly by adsorbed oxygen and/or lattice oxygen. The small amount of adsorption oxygen (O_2-TPD) may be responsible for the much higher catalytic activity of the nanoparticles at lower temperature. The great increase catalytic activity of the cubes at higher temperature can be attributed to the enhancement of $Mn^{3+} \rightarrow Mn^{4+}$ charge mobility.

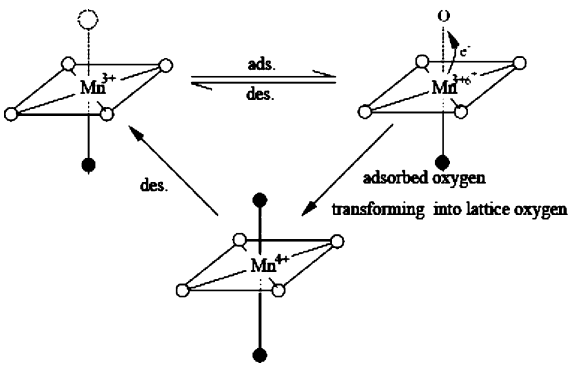

Figure 11. The scheme of oxygen transformation in the MnO_6 octahedral. Small open circles are oxygen I ions, small black circles are oxygen II ions, and large dotted-line open circles are oxygen vacancies.

5. Conclusions

$La_{0.5}Sr_{0.5}MnO_3$ cubes and nanoparticles with pseudo-cubic structures were synthesized. $La_{0.5}Sr_{0.5}MnO_3$ nanoparticles showed a higher activity for CO and CH_4 oxidation than the cubes at lower temperature, whereas the catalytic activity of the cubes significantly increased at higher temperature. The mechanism of CO oxidation over $La_{0.5}Sr_{0.5}MnO_3$ cubes was proposed. The adsorbed CO on Mn sites reacted with the lattice oxygen, and the chemisorbed oxygen transformed into the lattice oxygen to reinforce the consumed lattice oxygen. Jahn−Teller distortion controlled the catalytic activities of $La_{0.5}Sr_{0.5}MnO_3$ cubes and nanoparticles.

Acknowledgment. This work was partly supported by Chinese National Science Foundation (20433010, 20571047). We are grateful to professor He Hong of Eco-Environmental Sciences, Chinese Academy of Sciences (RCEES-CAS) for the CO−TPD, O_2-TPD and H_2-TPR data.

References and Notes

(1) Rao, C. N. R. *J. Phys. Chem. B* **2000**, *104*, 5877.
(2) Cimino, S.; Colonna, S.; Rossi, S. D.; Faticanti, M.; Lisi, L.; Pettiti, I.; Portaz, P. *J. Catal.* **2002**, *205*, 309.
(3) Jin, S.; Tiefel, T. H.; Cormack, M. M.; Fastnacht, R. A.; Ramesh, R.; Chen, L. H. *Science* **1994**, *264*, 413.
(4) Tian, Y.; Chen, D. R.; Jiao, X. L. *Chem. Mater.* **2006**, *18*, 6088.
(5) Mccarty, J. G.; Eise, H. *Catal. Today* **1990**, *8*, 231.
(6) Makamura, T.; Misono, M.; Yoneda, Y. *J. Catal.* **1983**, *83*, 151.
(7) Royera, S.; Alamdarib, H.; Duprezc, D.; Kaliaguinea, S. *Appl. Catal. B* **2005**, *58*, 273.
(8) Khromushin, I. V.; Aksenova, T. I.; Zhotabaev, Z. R. *Solid State Ionics* **2003**, *162−163*, 37.
(9) Jaenicke, S.; Chuah, G. K.; Bunsenges, B. *Phys. Chem.* **1992**, *96*, 1.
(10) Barnard, K. R.; Forger, K.; Turney, T. W.; Williams, R. D. *J. Catal.* **1990**, *125*, 265.
(11) Ponce, S.; Pena, M.; Fierro, J. *Appl. Catal. B* **2000**, *24*, 193.
(12) Viswanathan, B. *Catal. Rev. Sci. Eng.* **1992**, *34*, 337.
(13) Wang, L.; Zhu, Y. F. *J. Phys. Chem. B* **2005**, *109*, 5118.
(14) Zhou, K. B.; Wang, X.; Sun, X. M.; Peng, Q.; Li, Y. D. *J. Catal.* **2005**, *229*, 206.
(15) Zhou, K. B.; Wang, R. P.; Xu, B. Q.; Li, Y. D. *Nanotechnology* **2006**, *17*, 3939.
(16) Granado, E.; Sanjurjo, J. A.; Rettori, C.; Neumeier, J. J.; Oseroff, S. B. *Phys. Rev. B* **2000**, *62*, 11304.
(17) Gupta, R.; Sood, A. K.; Mahesh, R.; Rao, C. N. R. *Phys. Rev. B* **1996**, *54*, 14899.
(18) Spooren, J.; Rumplecker, A.; Millange, F.; Walton, R. I. *Chem. Mater.* **2003**, *15*, 1401.
(19) Spooren, J.; Walton, R. I.; Millange, F. *J. Mater. Chem.* **2005**, *15*, 1542.
(20) Urban, J. J.; Ouyang, L.; Jo, M. H.; Wang, D. S.; Park, H. K. *Nano Lett.* **2004**, *4*, 1547.
(21) Wang, X.; Na, N.; Zhang, S. C.; Wu, Y. Y.; Zhang, X. R. *J. Am. Chem. Soc.* **2007**, *129*, 6062.
(22) Breysse, M.; Claudel, B.; Faure, L.; Guenin, M.; Williams, R. J. J.; Wolkenstein, T. J. *J. Catal.* **1976**, *45*, 137.
(23) Shi, J. J.; Zhu, Y. F.; Zhang, X. R.; Baeyens, W. R. G.; Garcia-Campana, A. M. *Trends Anal. Chem.* **2004**, *23*, 351.
(24) Ponce, S.; Peña, M. A.; Fierro, J. L. G. *Appl. Catal. B* **2000**, *24*, 193.
(25) Vogel, E. M.; Johnson, D. W., Jr.; Gallagher, P. K. *J. Am. Ceram. Soc.* **1977**, *60*, 31.
(26) Ishihara, T.; Fukui, S.; Enoki, M.; Matsumotoa, H. *J. Electrochem. Soc.* **2006**, *153*, A2085.
(27) Rodriguez, J. A. *J. Phys. Chem.* **1994**, *179*, 5758.
(28) Xue, L.; Zhang, C. B.; He, H.; Teraoka, Y. *Appl. Catal. B* **2007**, *75*, 157.
(29) Hu, Y. H.; Ruckenstein, E. *J. Catal.* **1996**, *163*, 306.
(30) Luo, M. F.; Zhong, Y. J.; Yuan, X. X.; Zheng, X. M. *Appl. Catal. A* **1997**, *162*, 121.
(31) Yamazoe, N.; Teraoka, Y. *Catal. Today* **1990**, *8*, 175.
(32) Royera, S.; Alamdarib, H.; Duprezc, D.; Kaliaguinea, S. *Appl. Catal. B* **2005**, *58*, 273.
(33) Petrolekas, P. D.; Metcalfe, I. S. *J. Catal.* **1995**, *152*, 147.

(34) Podobedov, V. B.; Webet, A.; Romero, D. B.; Rice, J. P.; Drew, H. D. *Solid State Commun.* **1998**, *105*, 589.

(35) Pantoja1, A. E.; Trodahl, H. J.; Buckley, R. G.; Tomioka, Y.; Tokura, Y. *J. Phys. Condens. Matter* **2001**, *13*, 3741.

(36) Yamamoto, K.; Kimura, T.; Ishikawa, T.; Katsufuji, T.; Tokura, Y. *Phys. Rev. B* **2000**, *61*, 14706.

(37) Iliev, M. N.; Abrashev, M. V. *J. Raman Spectrosc.* **2001**, *32*, 805.

(38) Podobedov, V. B.; Weber, A. *Phys. Rev. B* **1998**, *58*, 43.

(39) Radaelli, P. G.; Cox, D. E.; Marezio, M.; Cheong, S. W. *Phys. Rev. B* **1997**, *55*, 3015.

(40) Zhou, H.; Shen, Y. F.; Wang, J. Y.; Chen, X.; O'Young, C. L.; Suib, S. L. *J. Catal.* **1998**, *176*, 321.

(41) Teng, F.; Liang, S. H.; Gaugeu, B.; Zong, R. L.; Yao, W. Q.; Zhu, Y. F. *Catal. Commun.* **2007**, *8*, 1748.

(42) Yang, X. M.; Luo, L. T.; Zhong, H. *Appl. Catal. A* **2004**, *272*, 299.

(43) Lou, H.; Zhen, H.; Yang, J.; Yao, Z.; Yu, S.; Ma, F. *Chem. J. Chin. Univ.* **1995**, *16*, 107.

(44) Arai, H.; Yamada, T.; Eguchi, K.; Seiyama, T. *Appl. Catal. A* **1986**, *26*, 265.

(45) Alifanti, M.; Kirchnerova, J.; Delmon, B.; Klvana, D. *Appl. Catal. A* **2004**, *262*, 167.

(46) Alifanti, M.; Kirchnerova, J.; Delmon, B. *Appl. Catal. A* **2003**, *245*, 231.

(47) Marchetti, L.; Forni, L. *Appl. Catal. B* **1998**, *15*, 179.